The International Journal of Advanced Manufacturing Technology (2019) 105:637–649
https://doi.org/10.1007/s00170-019-04193-0

ORIGINAL ARTICLE

Emissivity calibration method for pyrometer measurement of melting pool temperature in selective laser melting of stainless steel 316L

Chi-Guang Ren[1] · Yu-Lung Lo[1] · Hong-Chuong Tran[1] · Min-Hsun Lee[1]

Received: 12 April 2019 / Accepted: 23 July 2019 / Published online: 13 August 2019

Abstract
Selective laser melting (SLM) is an additive manufacturing (AM) technique for producing arbitrary work pieces, in which a laser beam is controlled to melt specific regions of a metal powder bed layer by layer so as to build up the required geometric form. In the present study, a method is proposed for calibrating the measurements obtained by a pyrometer for the melting pool temperature in the SLM of stainless steel 316L powder using the estimated values of the emissivity coefficients obtained from finite element heat transfer simulation and experimental tests. The accuracy in temperature prediction by heat transfer simulation is also confirmed by embedding a thermocouple into the powder bed. As a result, the calibration process is applicable to both one-color and two-color pyrometry methods. It is shown that the average error between the temperature measurements obtained from the calibrated pyrometer and the simulated temperature is just 1%. In other words, the feasibility of the proposed emissivity-based calibration method is confirmed. In the author's knowledge, this is the first proposed idea to calibrate the emissivity of the pyrometer based upon the simulation model for accurately extracting the true melting pool temperature.

Keywords Emissivity · Pyrometer · Melting pool · Selective laser melting

1 Introduction

The physical phenomena associated with the SLM process is extremely complex, and the quality of the final product depends on many factors, including the laser power, the laser spot size, the scan speed, the hatch distance, the melting pool area, the melting pool temperature, and the powder size distribution [1, 2]. Among these various factors, the temperature distribution of the melting pool has one of the most critical effects on the SLM outcome. Hence, measuring the temperature of the melting pool using noncontact measurement methods such as radiation thermometry or pyrometry is of great practical concern. For instance, the authors in literatures [3, 4] employed an infrared camera to capture the radiant temperature information during the SLM processing using Inconel 718 powder. The width and length of the melt pool were extracted based on the process of identification of the liquidus and solidus transition. Furthermore, studies in [5] used a high-speed infrared camera to investigate the effect of laser power and scanning speed on the temperature distribution, temperature gradients, and heating/cooling rates in and around the melt pool during the SLM process. In addition, the collected images from the infrared camera were used to calculate the speed of ejection particles.

The application of pyrometry to laser additive manufacturing was first reported around the year 2000 [6–8] and involved the use of pyrometers to observe the melting pool temperature online and provide a feedback signal for process control purposes. In later studies, pyrometers were used with specific cameras to obtain not only the temperature of the melting pool but also its geometry [9, 10]. The literature contains many studies on the use of pyrometers to investigate the SLM process [11]. Additionally, many pyrometer-based optical systems for melting pool analysis have been proposed [12–14]. Importantly, the pyrometer signal provides the means not only to monitor the on-going SLM process but also to evaluate the product quality. As a result, it plays a crucial role in optimizing the SLM process. For example, Furomoto et al. [15] used a two-color pyrometer to investigate the consolidation

✉ Yu-Lung Lo
loyl@mail.ncku.edu.tw

[1] Department of Mechanical Engineering, National Cheng Kung University, Tainan, Taiwan

mechanism of metal powders. Recently, Reken et al. [16, 17] used the pyrometer to measure the average temperature of the melt pool during the SLM process. The feedback signal from the pyrometer was used to control the laser power to minimize the variation of the temperature of the melt pool during the manufacturing process. However, to obtain accurate temperature measurements using a pyrometer, the emissivity of the target surface must first be estimated. In practice, this is extremely difficult due to phase transition effects. Furthermore, the measured temperature depends not only on the surface emissivity but also on the window transmissivity [18]. Consequently, the estimation process becomes even more complicated when the pyrometer is integrated with the laser scanning system of an SLM machine since the transmissivity of the coating materials in the optical system must also be considered.

In [10, 13], the authors presented a method for using the pyrometer signal to detect SLM part failure. However, the pyrometer was not calibrated and the pyrometer readings were given only in arbitrary units. Chivel and Smuro [12] used a pyrometer and a CCD camera to observe the maximum temperature and temperature distribution of the SLM melting pool and to calibrate the surface temperature distribution. However, the monitoring system indicated only the brightness and color temperature of the target surface. Furumoto et al. [15] proposed an emissivity-based calibration method for improving the accuracy of two-color pyrometer measurements of the temperature of the consolidated zone in the SLM process. However, the irradiated heat sources considered in the calibration process were emitted from a bulk material rather than the heat-affected zone (HAZ). Hence, the emissivity of the actual melting pool area was not estimated, and thus the accuracy of the calibration process was degraded. Doubenskaia et al. [19] used a monitoring system comprising a two-color pyrometer and a CCD camera to observe the melting area, although the pyrometer signal from the HAZ could be used to evaluate the effects of the SLM process parameters on the melting pool temperature. However, the pyrometer measurements were available only in arbitrary units due to the problems involved in integrating the proposed optical system with a commercial SLM machine.

In order to overcome the limitations described above, this study proposes a new emissivity-based calibration method for estimating the true temperature of the SLM melting pool. The calibration method is based on the temperature distribution data obtained from COMSOL simulations of the melting pool and experimental tests, respectively. Notably, the proposed calibration method is applicable to both one-color and two-color pyrometry methods. Moreover, the proposed method takes the incident angle θ of the pyrometer relative to the powder bed into account in the one-color mode, thereby improving the accuracy of the calibration results. The feasibility of the proposed method is demonstrated by comparing the experimental results for the melting pool temperature of stainless steel 316L in the SLM process with the simulated temperature.

2 Modeling and simulation of heat transfer during the SLM process

In this study, the heat transfer in the powder layer during the SLM process is investigated by means of COMSOL simulations. In the SLM process, as the laser beam irradiates the powder bed, the laser energy will propagate through the powder bed due to multiple reflections between laser radiations and powder particles [20]. Consequently, the laser energy density in the present simulation can be modeled as volumetric heat source rather than a surface heat flux [21]. This simulation also took into account the temperature-dependent properties of stainless steel 316L (e.g., thermal conductivity, density, and heat capacity) and the latent heat of fusion. In addition, the three-dimensional heat conduction equation was employed to describe the heat transfer within the powder layer. The details of the simulation process are described in the following subsections.

2.1 Volumetric heat source modeling

Figure 1 demonstrates the schematic views describing the initial, boundary condition, and geometry for the finite element (FE) heat transfer in the present study. The equations for modeling the energy density of a Gaussian laser beam can be written as [22]

$$q(r) = \frac{2P}{\pi r_0^2} \exp\left(\frac{-2r^2}{r_0^2}\right) \tag{1}$$

where P is the laser power, r_0 is the radius of the laser beam at which the laser energy diminishes to $1/e^2$, and r is the radial distance from a point on the powder bed surface to the center of the laser spot. Assuming that the laser beam scans the powder bed surface with a constant speed v for time t, according to Fig. 1, Eq. (1) can be written in (x,y) coordinate form as [23]

$$q(x,y,t) = \frac{2P}{\pi r_0^2} \exp\left[-\frac{2\left((x-vt)^2 + y^2\right)}{r_0^2}\right] \tag{2}$$

When the laser beam irradiates the metal powder layer, part of the incident energy is absorbed and transfer along the thickness of the powder layer. The distribution of the absorbed

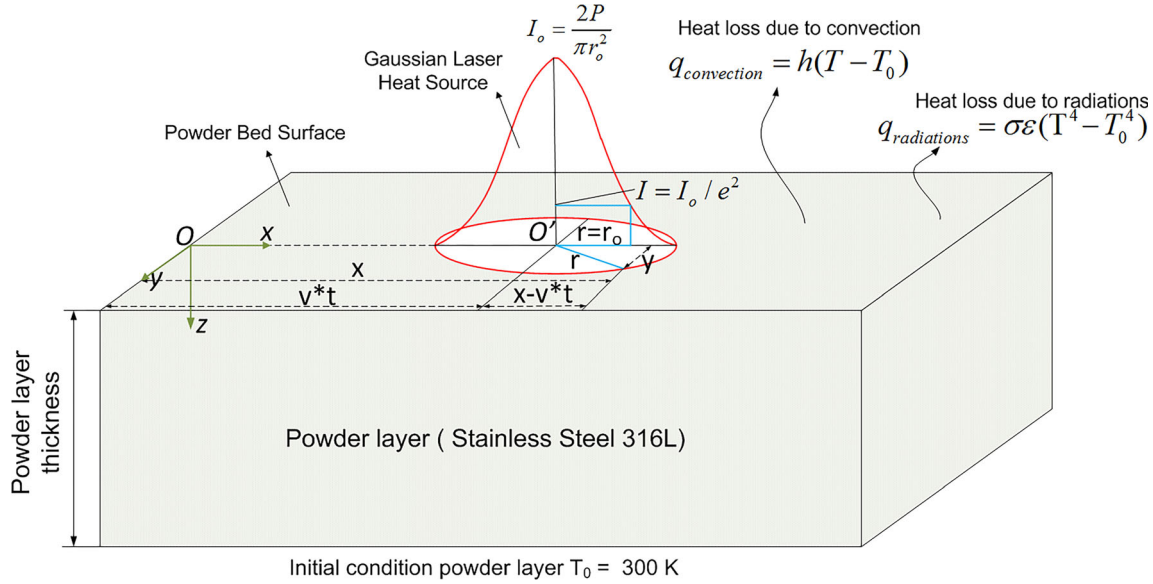

Fig. 1 Schematic diagram of the simulation setup

energy depends strongly on the powder size distribution as well as the thickness of the powder bed [24]. Consequently, the effects of the powder size distribution and powder layer thickness were modeled using the volumetric heat source equations proposed in [21], i.e.,

$$q(x,y,z,t) = \frac{2P}{\pi r_0^2}\exp\left[-\frac{2\left((x-vt)^2+y^2\right)}{r_0^2}\right]\frac{dA}{dz} \tag{3}$$

where $\frac{dA}{dz}$ is the rate of change of the absorptivity profile along the depth direction of the powder layer. (Note that the detailed derivation of $\frac{dA}{dz}$ is described in [21] and is hence omitted here.)

2.2 Material properties of stainless steel 316L powder

In the SLM process, the material properties of powder bed undergoes pre-melting stage and melting stage. The effective thermal conductivity of the powder bed at temperatures lower than the melting point of stainless steel 316L (1648 K) was calculated using the model proposed in [21] based on the simulation results obtained for the packing density and average coordination number, respectively. Additionally, from the calculated packing density of the packed bed, the density of the powder layer in the pre-melting stage can be calculated by the equation specified in [21]. For temperatures higher than the melting point, the thermal conductivity and density were simply assigned the same value as that of the bulk material. When it comes to the specific heat of the powder bed, the powder layer in the SLM process comprises a mixture of solid phase and gas phase. However, the density and specific heat of the gas phase are just $\rho_{gas} = 1.2$ kg/m^3 and $c_{gas} = 1$ kJ/(kgK), respectively [25]. Thus, for simplicity, the specific heat of the powder bed was approximated to that of the bulk material.

2.3 Governing equations and conditions

The governing differential equation for three-dimensional nonlinear heat transfer in a material with isotropic thermal properties has the form [26]

$$\rho c\frac{\partial T}{\partial t} = q(x,y,z,t) + \frac{\partial}{\partial x}\left(k\frac{\partial T}{\partial x}\right) + \frac{\partial}{\partial y}\left(k\frac{\partial T}{\partial y}\right) + \frac{\partial}{\partial z}\left(k\frac{\partial T}{\partial z}\right) \tag{4}$$

where ρ is the material density (kg/m^3), c is the specific heat capacity (J/kgK), T is the temperature (K), t is the application time of the heat source (s), k is the thermal conductivity (W/(m·K)), and $q(x, y, z, t)$ is the heat generation per unit volume (W/m^3). In the present study, the powder layer was assumed to be at room temperature (300 K) initially. Moreover, the radiative cooling (Eq. (5)) and convective cooling (Eq. (6)) were applied as the boundary condition on the top surface of the powder layer [29, 32], i.e.,

$$Q_{\text{rad}} = -\sigma\epsilon\left(T^4 - T_a^4\right) \tag{5}$$

$$Q_{\text{conv}} = -h_c(T - T_a) \tag{6}$$

where T is the temperature of the powder bed, T_a is the ambient temperature, $\sigma = 5.669 \times 10^{-8}$ W/m^{2}K^4 is the Stefan constant, ϵ is the emissivity (0.4 for solid state and 0.1 for molten material), and $h_c = 100$ W/m^{2}K is the heat transfer coefficient.

3 Verification of the heat transfer model with thermocouple

The main purpose of the thermocouple experiments is to verify the reliability of the heat transfer model with the volumetric heat source [21] in predicting the temperature of the powder bed. In our previous studies in [21], by using the

volumetric heat source that took into account the powder size distribution and the powder layer thickness on the distribution of laser energy density along the depth of the powder bed, we can obtain the calculated temperature which was in better agreement with the experimental results than those obtained in literatures [27, 28]. Thus, the heat transfer modeling developed by our group is used for calibration of a pyrometer in measuring the average temperature in the melting pool.

3.1 Simulation model for verifying thermocouple experiments

As illustrated in Fig. 2, the thermocouple is embedded inside the powder bed and just located beneath the surface of the powder bed around 200 μm. In simulation, the sequential addition model proposed by our group in [24] was first employed to simulate the powder layer. The simulated powder size distribution and the corresponding simulated powder bed are shown in Fig. 3 a and b, respectively. It is noted that the thickness of the simulated powder layer is set as 0.7 mm which is the same as the experimental conditions. It is time consuming to simulate the powder bed if the length and width are the same as the experimental settings. Therefore, in choosing the length and width for the powder bed in simulation, these two dimensions were gradually increased until the calculated absorptivity in ray tracing simulation reached the convergence value. In particular, the length and width of the simulated powder bed were set as 0.5 mm. The geometry details of the simulated powder bed were imported into Zemax software to perform Monte Carlo ray tracing simulation for calculating the absorptivity profile along the depth of the powder bed. Notably, detail of the procedure to calculate the absorptivity profile along the depth of the powder bed was specified in our previous work in [21]. Figure 4 a shows the snapshot of ray tracing simulation. From Fig. 4a, it is observed that as the laser beam irradiated the powder bed, the laser energy is dissipated based on two mechanisms which are absorption and scattering. In the former mechanism, part of laser energy is absorbed and penetrates inside the powder bed due to multiple reflections between laser radiations and powder particles. In the latter mechanism, the remaining energy of the laser beam is scattered back from powder particles outward and cannot be absorbed anymore.

Figure 4 b shows the corresponding calculated absorption profile regarding the thickness of the powder layer. It is seen that as the laser beam irradiates the powder bed, the absorbed energy is distributed from the top surface of the powder layer to the depth at $z = 55$ μm. Interestingly, it is observed that although the laser beam irradiated on the top surface of the powder layer, the absorptivity at $z = 70$ μm is actually lower than that at $z = 67$ μm (i.e., a position slightly below the top surface of powder bed). This observation is reasonable because the absorptivity at the top surface of the powder bed is contributed by the laser energy irradiated by the laser source directly. On the contrary, at $z = 67$ μm, the absorbed energy includes both the energy irradiated by the laser source and the energy of laser radiations reflected by the powder particles within the powder layer. Notably, this observation is consistent with simulation findings illustrated in the literatures [29, 30].

The simulation parameters in the FE heat transfer model are listed in Table 1. Through conducting a series of convergence trials, the mesh size was chosen as 16 μm and the type of element is hexahedron. The simulation did not consider the phase change of evaporation because the experiment is conducted with a low laser power. Based on the results of simulation and experiment, the melt pool's peak temperature of the SS 316L powder bed was not over the evaporation point (3200 K). As the thermocouple only measured the temperature during the heating stage of laser (around 2000 ms), therefore, the present simulation does not consider the cooling stage after turning off the laser. In Fig. 5, the simulated peak temperature in the melting pool is around 2665 K by the end of the applying time of the laser. It is noted that the laser applying time is almost equal to the time at which the measured temperature from the thermal couple reached a steady state. As shown in Fig. 5, the point located at the center of the thermocouple sensor is equal to 1769.3 K in the simulation, and that obtained from the experiment is 1703.9 K. Therefore, it can be concluded that the simulated results have good agreement with the experimental data. The detail of experimental setup is described in the next paragraph.

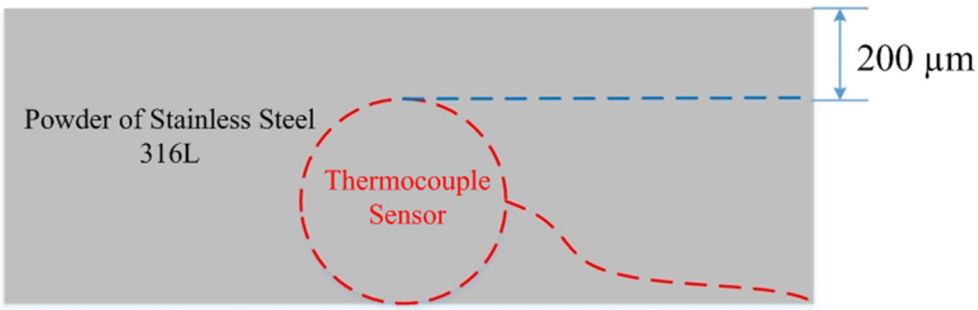

Fig. 2 Illustration of thermocouple experiment

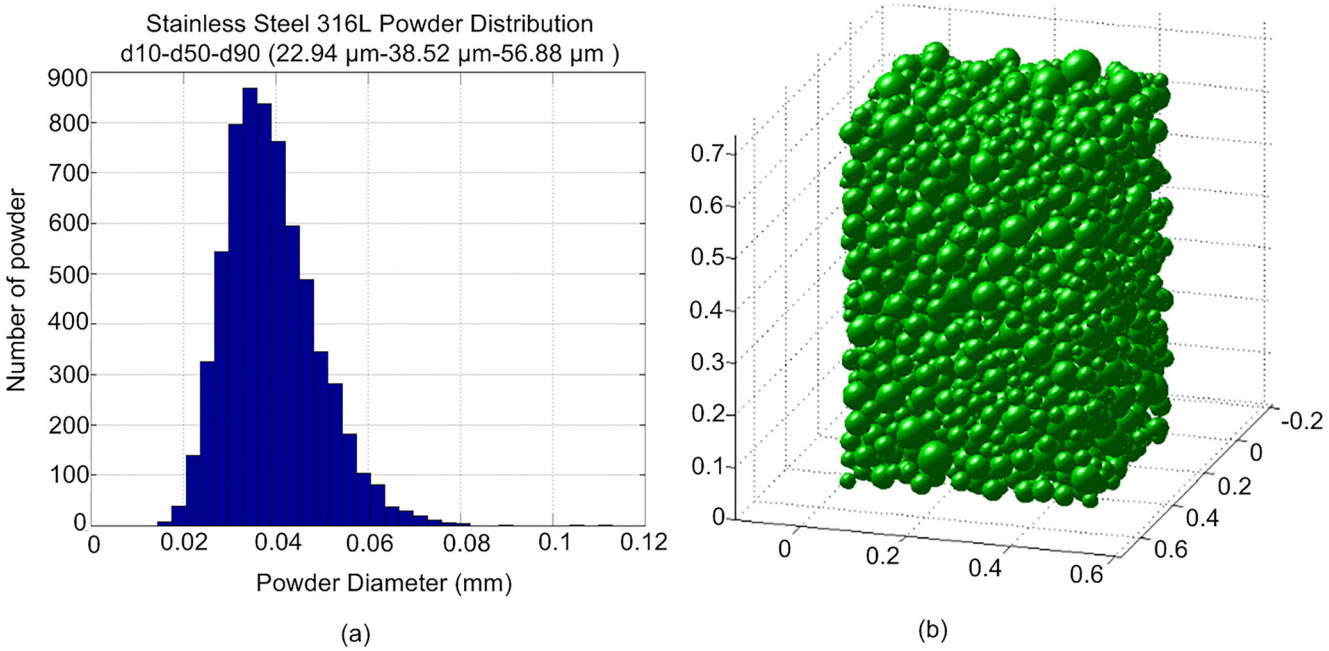

Fig. 3 **a** Powder distribution of SS 316L. **b** Powder layer raining model with dimension $0.5 \times 0.5 \times 0.5 \times 0.7$ mm^3

3.2 Experimental setup of the thermocouple embedded inside the powder bed

The experiments are conducted on a commercial Tongtai AM-250 SLM machine with a Nd-YAG laser with a wavelength of 1064 nm, a maximum laser power of 500 W, and a D4 sigma laser beam diameter of 120 μm. The size distribution of the SS 316L powder is 22.94–36.52–56.88μm ($d_{10} - d_{50} - d_{90}$), and the material of the substrate is SS316L. The R type thermocouple was employed with the 2000-K melting point, and the dimension of the thermocouple sensor is around 500 μm in diameter. The temperature recorder of the thermocouple chosen was GL829 (Graphtec Co., Japan) with a sampling times of 100 ms. Figure 6 shows the experimental setup in which the thermocouple is embedded into the powder bed with 200 μm beneath the surface. It is noted that the thickness of the metal powder layer is 700 μm.

In the process of the experiment, it is noted that the thermocouple was employed to measure the temperature when the melting pool reaches the beginning point of the steady temperature in a transient state. By doing so, it can eliminate the effect of response time of the temperature recorder which is 100 ms and also the time of heat conduction in the thermocouple for measuring the steady temperature. The dimension of the R-type thermocouple sensor is 500 μm, which is approximately ten times larger than the metal powder in diameter. Therefore, the measured temperature is not on single point but an average temperature over the region of the circular thermocouple. In Fig. 7, the experimental result reveals that the average temperature to reach a steady temperature zone needs 0.7 s during the whole heating time in 2 s, and the average temperature measured as 1703.9 K is found when the melting pool reaches the beginning point of the steady temperature in a transient state. As a result, the average temperature extracted by a thermocouple at 1703.9 K has a good agreement with the simulation data of 1769.3 K as illustrated in Fig. 5. Accordingly, the experiment proves that the volumetric heat source [21] has great credibility in predicting the average temperature in the melting pool during the SLM process.

It is concluded that the first step to verify the reliability of the heat transfer simulation in the FE model mentioned in Sect. 3 by using thermocouple embedded into the powder bed is confirmed, then the pre-processing to calibrate the two-color pyrometer using the heat transfer simulation in the FE model is applied in order to accurately and quantitatively measure the temperature in the melting pool, and this is much different from the other groups only using experiments in calibration of the pyrometer for qualitative measurements. The new calibration using the heat transfer simulation in the FE model for a pyrometer will be introduced in the next sections.

4 Emissivity calibration of the pyrometer

According to [18], the measured temperatures in one-color mode and two-color mode of a pyrometer are expressed in Eqs. (7) and (8), respectively, as

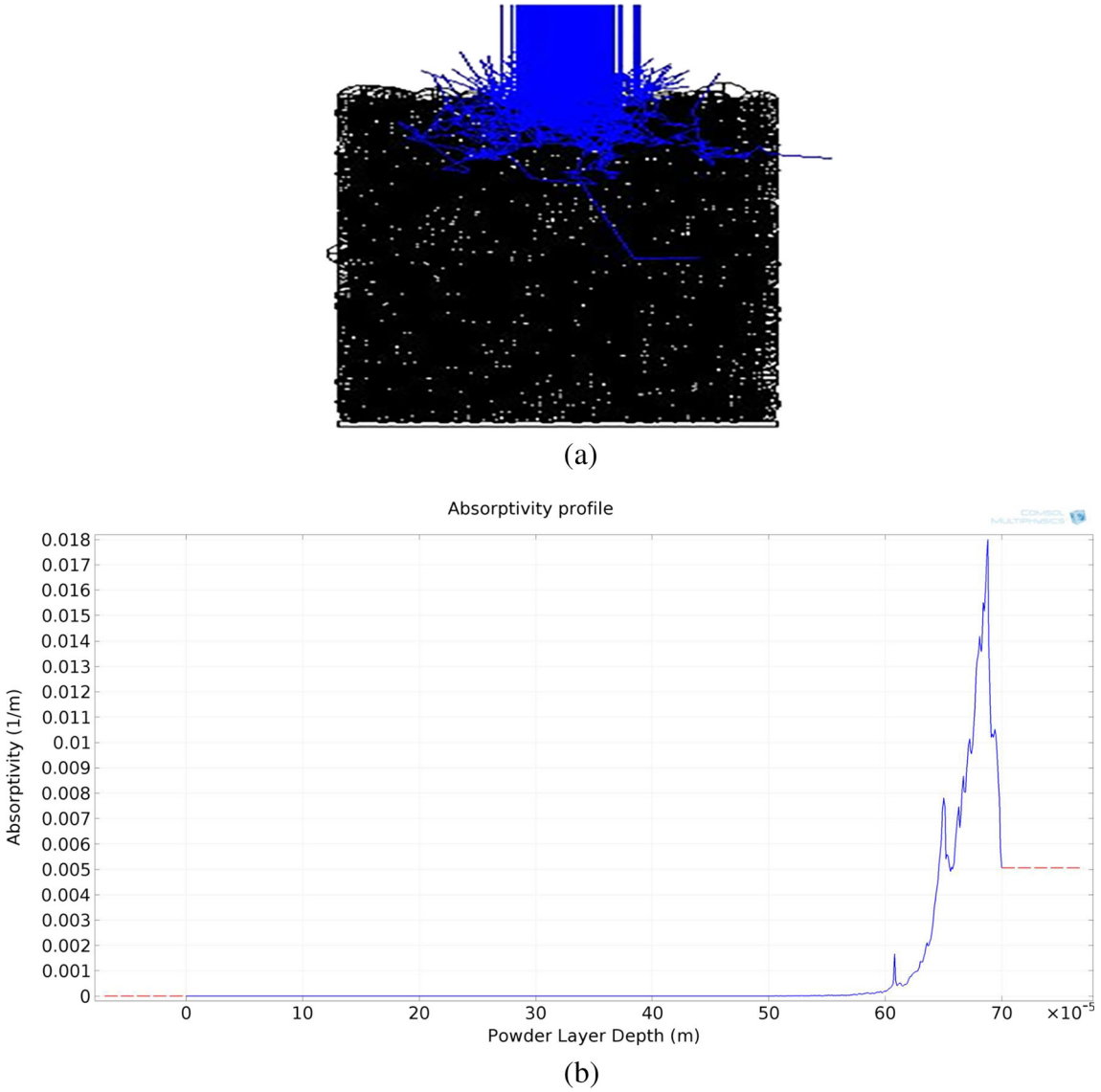

Fig. 4 **a** Ray tracing in the powder bed. **b** Calculated absorptivity profile along the 700-μm depth of powder layer thickness

$$\frac{1}{T_{1Ce_i}} = \frac{1}{T_{\lambda_i}} + \frac{\lambda_i}{c_2}\ln\varepsilon_{\lambda_i} \tag{7}$$

$$\frac{1}{T_{2Ce}} = \frac{1}{T_{\mathrm{ar}}} - \frac{\lambda_1\lambda_2}{c_2(\lambda_1-\lambda_2)}\ln\frac{\varepsilon_{\lambda_2}}{\varepsilon_{\lambda_1}} \tag{8}$$

where T_{1Ce_i} is the measured temperature from channel ith ($i = 1, 2$) of a pyrometer, λ_i is the effective (mean) wavelength of the ith ($i = 1, 2$) pyrometer spectral range, T_{λ_i} is the apparent temperature associated with λ_i, and ε_{λ_i} is the emissivity of the target surface at λ_i. In addition, T_{2Ce} is the measured temperature from the two-color mode of a pyrometer, T_{ar} is the apparent ratio temperature, and c_2 is the second radiation constant, which is equal to 14387.69 μm K [18]. It is noted that the apparent temperature, T_{λ_i}, and the apparent ratio temperature, T_{ar}, are the built-in data in a pyrometer. Thus, in order to obtain the channel temperature, T_{1Ce_i}, in a one-color mode operation, and the (true) temperature, T_{2Ce}, in a two-color mode operation, the emissivity coefficients need to be obtained in advance.

In the present SLM trials, the temperature of the HAZ was measured by a two-color pyrometer (Model H322, Sensortherm GmbH, Germany) with a temperature range of 1273 − 2773 K; two InGaAs detectors; spectral ranges of 1.65 − 1.80 μm and 1.40 − 1.65 μm for channel 1 and channel 2, respectively; a sampling time of 40 μs; and a measurement area with a diameter of 1.65 mm at a working distance of 600 mm. The pyrometer field of view is much larger than the HAZ (typically around 760 μm in diameter for a laser beam radius of 60 μm and a scanning speed of 0 mm/s) in SLM process. This condition violates the intended operating principle of pyrometers, in

Table 1 Simulation parameters in FE heat transfer simulation

Parameters	Value
Laser power (W)	15
Laser radius (μm)	60
Laser applying time (s)	0.7
Dimension of powder layer	1200 × 1200 × 700 μm
Mesh type	Hexahedron
Mesh size (μm)	16
Melting point (K)	1648
Material	Stainless steel 316 L
Latent heat of fusion (kJ/kg)	300

Fig. 6 Experimental setup in the thermocouple

which the field of view is expected to be far smaller than the target area. Consequently, the temperature measurements directly obtained using the pyrometer without any correction are unreliable, particularly when the pyrometer is operated in the one-color mode, in which the temperature reading is strongly dependent on the filling area, which means the surface area of the heat-affected zone, and surface emissivity [18]. As a result, previous studies on the use of pyrometers for monitoring and controlling the SLM process report the melting pool temperature using only brightness temperature values or arbitrary units [13, 19]. In practice, however, detecting the true melting pool temperature is essential in properly controlling the SLM process and ensuring the quality of the final product.

Accordingly, the present study proposes an emissivity calibration technique based on the temperature field data obtained from COMSOL simulations and experimental tests to determine the true temperature of the melting pool from the pyrometer measurements. The proposed calibration technique is applicable to both one-color and two-color pyrometry techniques and takes the incident angle θ of the pyrometer relative to the powder bed into account. In the one-color measurement mode, the temperature, T_{1C}, is formulated as

$$T_{1C} = \frac{N_{HAZ}\overline{T}_{HAZ} + (N_P - N_{HAZ}) \times 1273}{N_P} = \frac{N_{HAZ}}{N_P}\frac{\sum_{i=1}^{N_{HAZ}} T_i}{N_{HAZ}} + \left(1 - \frac{N_{HAZ}}{N_P}\right) \times 1273$$
$$= \frac{A_{HAZ}}{A_P}\frac{\sum_{i=1}^{N_{HAZ}} T_i}{N_{HAZ}} + \left(1 - \frac{A_{HAZ}}{A_P}\right) \times 1273, \quad (9)$$

where N_{HAZ} is the number of nodes in the HAZ having a temperature greater than 1273 K (the minimum temperature the pyrometer is able to measure) and N_P is the total number of nodes within the measuring spot of the

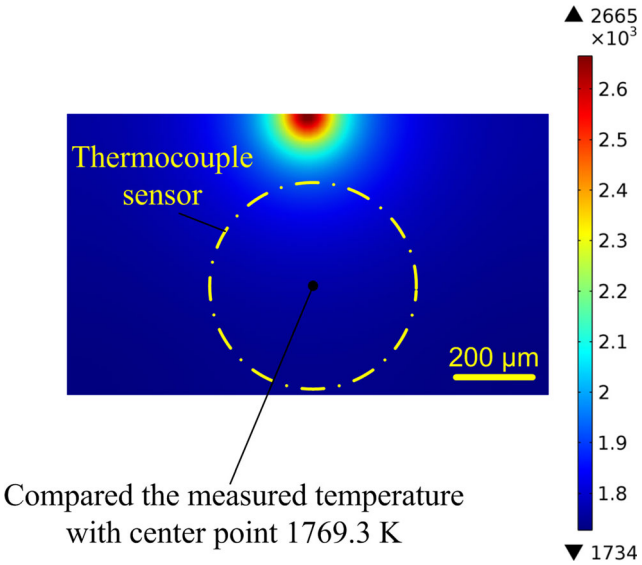

Fig. 5 The cross section of the center

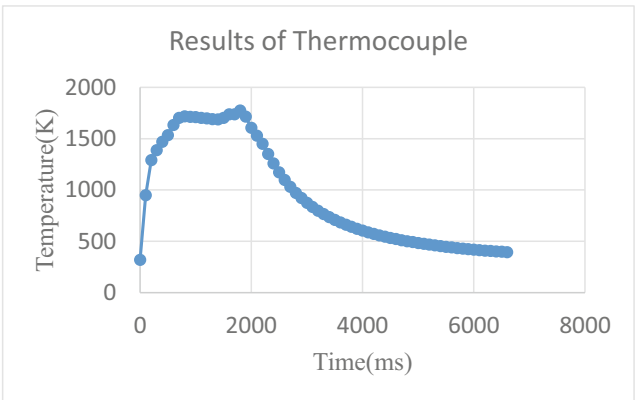

Fig. 7 Experimental results from thermocouple

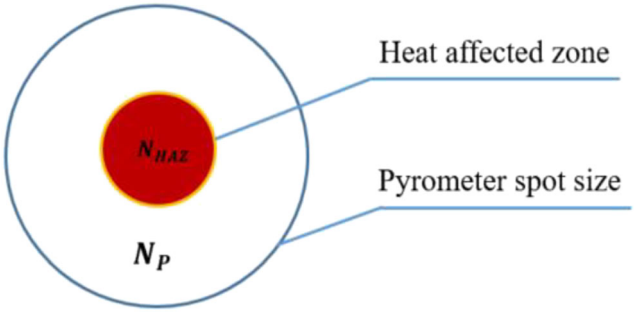

Fig. 8 Schematic illustration of HAZ and pyrometer spot size

pyrometer (see Fig. 8). In addition, A_{HAZ} is the area of the HAZ containing nodes with a temperature higher than 1273 K, A_{P} is the measuring spot size of the pyrometer, T_i is the temperature values of the nodes in the HAZ, and $\overline{T}_{\mathrm{HAZ}}$ is the average temperature of the HAZ.

When the pyrometer is arranged at an angle of 45° to the target surface, the measuring spot has the form of an ellipse, as illustrated in Fig. 9. Thus, the area of the target surface within the field of view of the pyrometer should be reformulated as follows:

$$A_P = \pi \frac{R}{\sin 45^{\circ}} R = \frac{\pi R^2}{\sin 45^{\circ}} \tag{10}$$

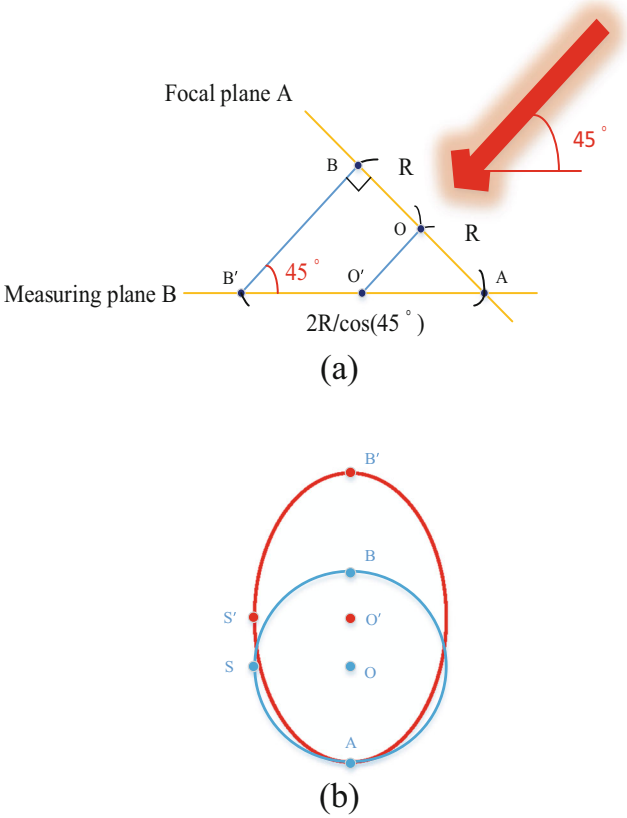

Fig. 9 Projections of the pyrometer focal plane on the powder bed in **a** the incident plane and **b** powder bed plane

where R is the radius of the pyrometer spot in the focal plane. A simple inspection of Eqs. (9) and (10) shows that the computed temperature in the one-color pyrometer mode reduces as the area A_{P} increases by a coefficient of $1/\sin 45^{\circ}$.

From the discussions above, the measured temperature in the one-color mode is strongly dependent on the area filling factor ($A_{\mathrm{HAZ}}/A_{\mathrm{P}}$). However, the area filling factor can be eliminated in the two-color (ratio) mode, and the temperature of the two-color mode pyrometer is given simply as

$$T_{2\mathrm{C}} = \frac{\sum_{i=1}^{N_{\mathrm{HAZ}}} T_i}{N_{\mathrm{HAZ}}} \tag{11}$$

Figure 10 presents a flowchart showing the detailed steps in the proposed emissivity-based calibration process. As shown, the one-color and two-color mode temperature values described above (i.e., $T_{1\mathrm{C}}$ and $T_{2\mathrm{C}}$, respectively) are first computed via FEM/COMSOL simulations. The emissivity coefficient of each channel of the pyrometer is estimated and adjusted in Eq. (7) in the one-color mode by comparing the simulated temperature values with the experimental data. It is noted that T_{λ_i} (i.e., the apparent temperature) in Eq. (7) is unknown and built-in in a pyrometer, so the emissivity $\varepsilon_{\lambda i}$ cannot be inferred directly, but adjusted iteratively. If the measured one-color mode temperature could not get close to the simulated one, the experiment to find the new ε_{λ_1} and ε_{λ_2} in emissivity of the one-color mode must be conducted again. Subsequently, using an emissivity ratio of $\varepsilon_{\lambda_2}/\varepsilon_{\lambda_1}$, the two-color pyrometer mode is employed to extract the experimental value of T_{2Ce} based upon Eq. (8). It is noted that the emissivities ε_{λ_1} and ε_{λ_2} are already obtained from the previous step, so in this step after the emissivity ratio is set, the (true) temperature can be measured without any emissivity estimation or adjustment. The extracted value is then compared with the simulated value, $T_{2\mathrm{C}}$. If the two values, T_{2Ce} and $T_{2\mathrm{C}}$, are in good agreement, the calibration process is terminated and the experimental temperature value is taken as the true HAZ temperature. However, if the measured two-color mode temperature could not get close to the simulated one, the experiment to find the new emissivities will be conducted again starting from the one-color mode operation.

5 Simulation and experimental setup for a pyrometer calibration

Table 2 summarizes the parameters used in COMSOL heat transfer simulation. Notably, the parameters were set in such a way that the formation of the melt pool is dominated by the conduction mode. In order words, the chosen parameters will not lead to the formation of the melt pool in the key-hole

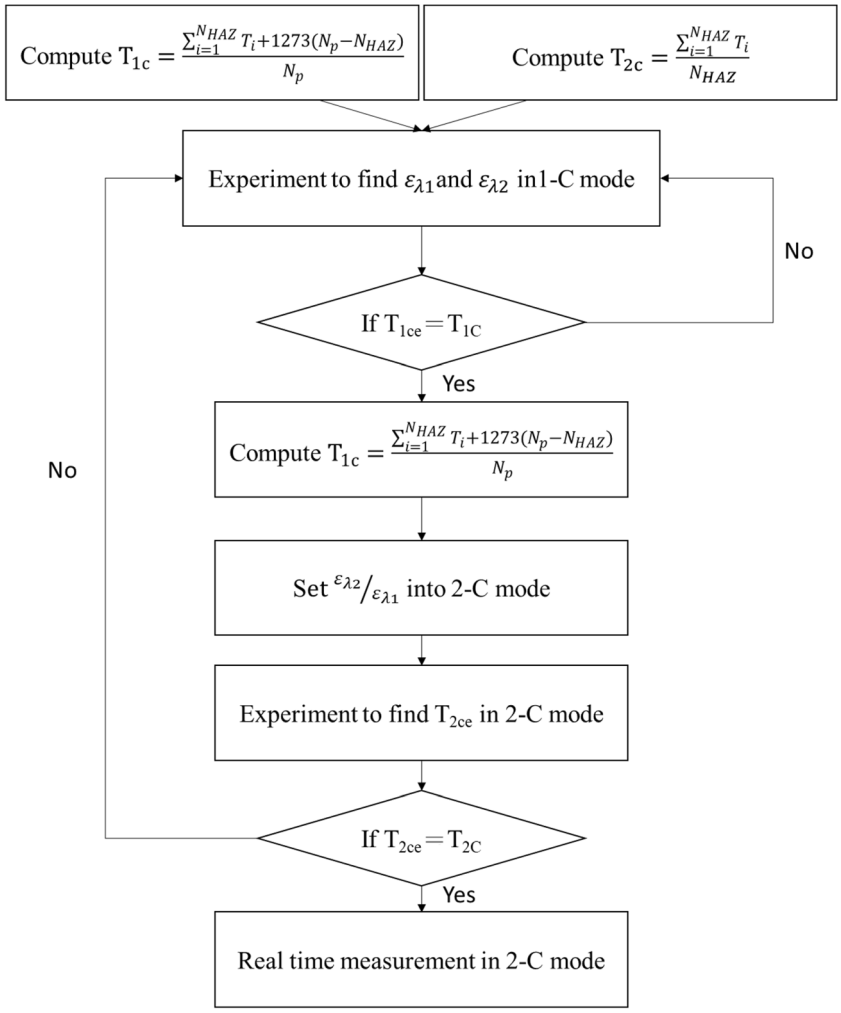

Fig. 10 Flowchart of the proposed emissivity-based calibration process

melting mode [31] which is driven by the Marangoni convection and vapor recoil pressure inside the melt pool. Accordingly, the heat transfer simulation model described in Sect. 2 is reasonably applied.

Table 2 Parameters used in COMSOL heat transfer simulations

Parameters	Value
Laser power (W)	15
Laser radius (μm)	60
Scan speed (mm/s)	0
Laser application time (s)	0.1
Dimensions of powder layer (μm × μm × μm)	1000 × 1000 × 200
Powder size distribution (μm − μm − μm)	d_{10}–d_{50}–d_{90} = 22.94–36.52–56.88
FE mesh type	Hexahedron
FE mesh size (μm)	10
Melting point (K)	1648
Material	Powdered stainless steel 316 L
Latent heat of fusion (kJ/kg)	300 [32]

In the experimental process, the pyrometer was installed on a tripod placed outside the SLM chamber. The pyrometer had a focal length of 600 mm and was arranged such that the measurement light was incident on the powder bed with an angle of 45°. From Eq. (8), A_P (i.e., the area of the pyrometer field of view on the powder bed) was found to be $\pi \times 0.95^2 \times 1/\sin 45^\circ$ mm^2. The stainless steel 316L powder layer thickness was set as 200 μm in order to prevent rapid heat dissipation from the melting pool to the substrate, thereby enabling more accurate measurements of the melting pool temperature to be obtained by the pyrometer. The laser scanning speed was set as 0 mm/s since the pyrometer was fixed in place after it was mounted on the tripod. In addition, the laser application time was set as 0.1 s in order to maintain the peak temperature of the melting pool for a sufficient time for its value to be acquired by the pyrometer.

5.1 Simulation results

The similar simulation procedure described in Sect. 3.1 was employed to simulate the temperature distribution. Figure 11

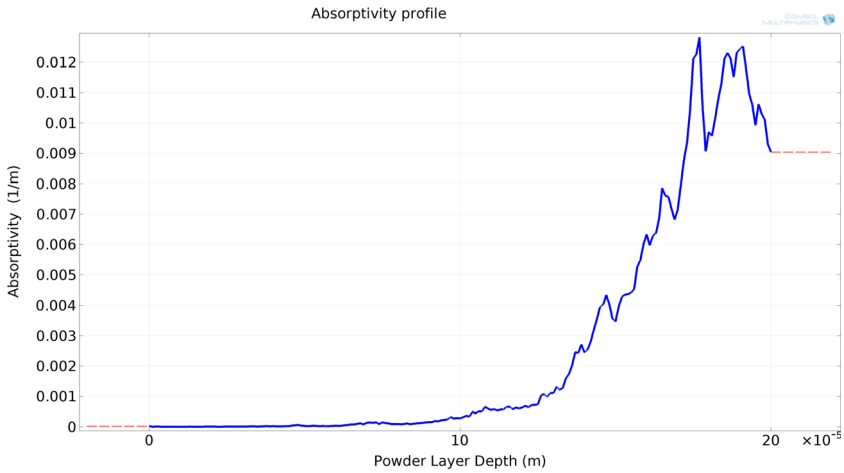

Fig. 11 Absorptivity profile along the thickness of the powder bed

shows the absorptivity profile of the powder bed, as computed using the model proposed in [21].

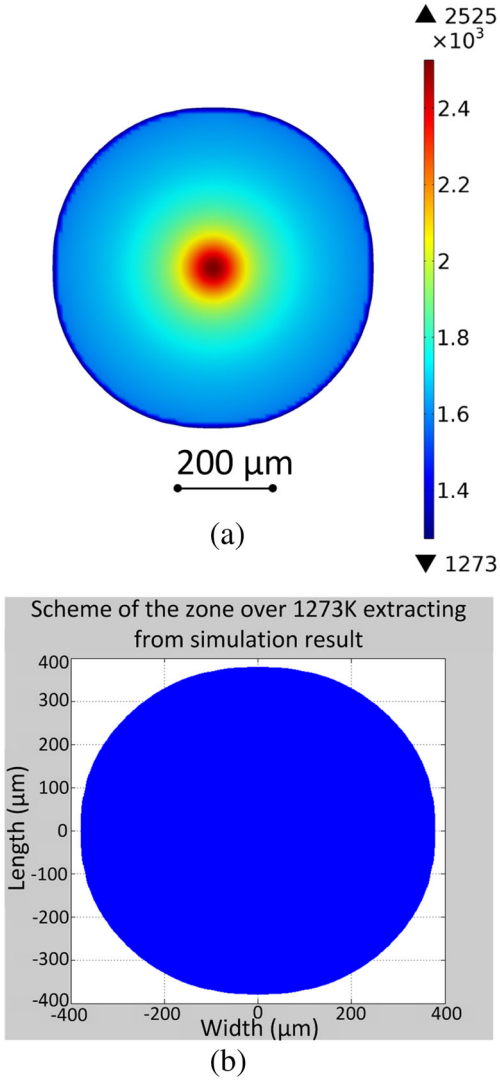

Fig. 12 COMSOL simulation results for **a** temperature distribution on the powder bed surface, and **b** region of the powder bed surface with temperature greater than 1273 K

Figure 12 a and b show the COMSOL simulation results for the temperature field on the upper surface of the powder bed and the region of the powder bed surface with a temperature higher than 1273 K, respectively. Note that in performing the simulations, the field of view of the pyrometer was specified as $A_P = \pi \times 0.95^2 \times 1/\sin 45^\circ$ mm^2 and the area of the HAZ was calculated as $A_{HAZ} = \pi \times 0.76^2$ mm^2. According to Eq. (9) and (11), the simulated temperatures for the one-color pyrometer mode (T_{1C}) and two-color pyrometer mode (T_{2C}) are 1329 K and 1701 K, respectively.

5.2 Experimental results

As shown in Fig. 10, the simulated temperature in the one-color mode, T_{1C}, was used to estimate the emissivities of the melting pool associated with the two wavelength ranges of the pyrometer channels, i.e., 1.65 − 1.80 µm and 1.45 − 1.65 µm, respectively. In particular, the emissivity coefficients were adjusted iteratively until the measured temperatures for the two wavelength ranges approached the simulated temperature, T_{1C}. The final values of the emissivity coefficients for channel 1 and channel 2 were found to be $\varepsilon_{\lambda_1} = 0.64$ and $\varepsilon_{\lambda_2} = 0.70$, respectively. Having estimated the two coefficients, ten separate measurements of the HAZ temperature were acquired in

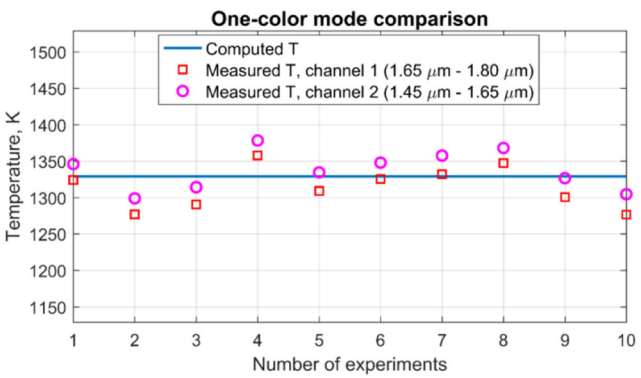

Fig. 13 Experimental temperature vs. computed temperature in one-color mode of a pyrometer

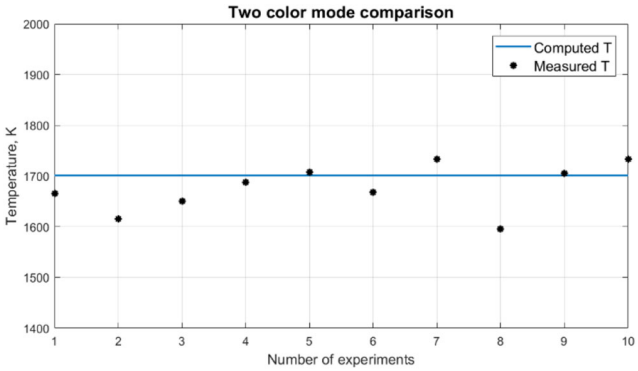

Fig. 14 Experimental temperature vs. computed temperature in the two-color mode

the one-color mode of a pyrometer. The corresponding results are presented in Fig. 13. The average temperature values for channel 1 ($\varepsilon_{\lambda_1} = 0.64$) and channel 2 ($\varepsilon_{\lambda_2} = 0.70$) are 1314.1 K and 1337.7 K, respectively. The deviations of the channel 1 and 2 measurements are ±14.9 K and ±8.7 K, respectively. In addition, the corresponding errors (i.e., $|T_{\text{measured}} - T_{\text{simulated}}| / T_{\text{simulated}}$) are 1.12% and 0.65%, respectively. In other words, the measurement errors are relatively small over the pyrometer measurement range (1273 − 2773 K). Consequently, the feasibility of the proposed calibration method for predicting the temperature obtained by the pyrometer in the one-color mode is confirmed.

Based on the emissivity coefficients obtained in the one-color operation mode, the emissivity ratio for the two-color operation mode was set as 1.093 (i.e., $\varepsilon_r = \varepsilon_{\lambda_2}/\varepsilon_{\lambda_1} = 0.70/0.64 = 1.093$). Ten further measurements of the HAZ temperature were acquired in the two-color mode, as shown in Fig. 14. The average measured temperature is equal to 1681.5 K, corresponding to an error of 1.14% compared with the simulated temperature of $T_{2C} = 1701$ K. In addition, the maximum error is found to be 6.22%, while the deviation is around ±105.8 K. Again, the good agreement between the simulated temperature value and the experimental temperature values confirms the effectiveness of the proposed calibration method for the two-color pyrometer operation mode.

Figure 15 shows the typical raw data obtained from the pyrometer software for the surface temperature (in K) over the duration of the laser application period. It is noted that while the sampling time of the pyrometer is 40 μs,the pyrometer software is able to handle a maximum sampling period of just 0.5 ms due to the limitations imposed by the USB connection and the computer in use. However, the results confirm that for a stationary laser beam, the chosen laser application time of 0.1 s is sufficiently slow for the pyrometer to successfully detect the peak HAZ temperature.

6 Conclusion and suggestions

This study has proposed an emissivity calibration technique for improving the accuracy of the temperature measurements obtained from a pyrometer for the fixed melting pool without a tail in the SLM processing of stainless steel 316L. In the proposed approach, the FE heat transfer simulation is first constructed to predict the temperature distribution of the melting pool in conduction melting mode, and then the simulated results are verified by comparing with the experimental data obtained from the thermocouple. Accordingly, the emissivity coefficients of the target surface are inferred via an iterative comparison between the experimental temperature measurements from a pyrometer and the predicted values obtained from COMSOL simulations.

Finally, the validity of the proposed calibration method has been demonstrated by comparing the experimental results for the HAZ temperature of the powder bed with the simulated

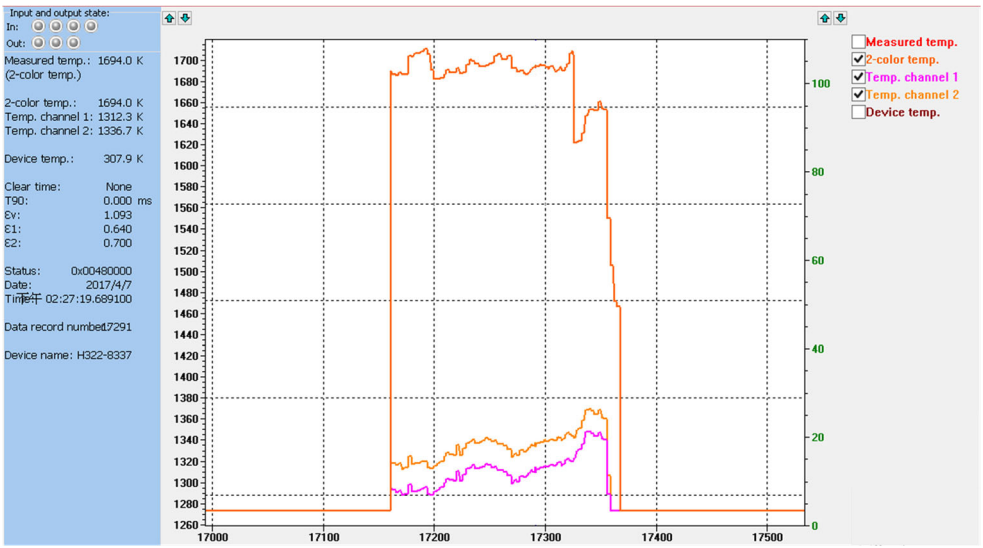

Fig. 15 Typical experimental raw data acquired from pyrometer software

values in both the one-color operation mode and the two-color operation mode from a pyrometer. It has been shown that the average error between the two sets of results is just 1%, while the maximum error is no more than 6%. In other words, the feasibility of the proposed calibration method for obtaining true temperature measurements of the melting pool in the SLM process is confirmed. To the best of the authors' knowledge, this is the newest proposed approach to calibrate the emissivity of the two-color pyrometer to accurately measure the average temperature of the melting pool.

For future works, the coaxial monitoring system including the two-color pyrometer will be built up and the proposed methodology will be employed to measure the average temperature of the moving melting pool with a tail. However, we may face the challenge described as follows. From our previous work in [21], it is known that the width of melting pool is comparable with the laser spot size and the melting pool length is in the order of several hundred microns to 1 mm, while the sensing area of the pyrometer has a diameter of 1.6 mm. Obviously, the average temperature of the moving melting pool would cover not only the temperature on the melting pool itself but also that on its tail if the sensing image of a pyrometer is larger than the area of the melting pool. However, the only average temperature on the melting pool measured by a pyrometer can be achieved by designing an additional co-axial optical system to focus the sensing image of a pyrometer just right inside the melting pool itself. As expected, by doing the way to focus on the very small area of the melting pool (the length of the melt pool is around 800 μm, and the width of melt pool is around 130 μm in a case that the laser beam radius is 120 μm) with a long distance around 1000 mm between an object and a pyrometer, more efforts need to be seriously made in stabilizing the SLM system to eliminate the noises in vibration.

Funding information This study was financially supported by the Ministry of Science and Technology of Taiwan under Grant No. MOST 107-2218-E-006-051. The research was also partially supported by the National Chung-Shan Institute of Science and Technology under an Aerospace-Grade Large-Scale Additive Manufacture Development and Verification Project.

References

1. Gibson I, Rosen DW, Stucker B (2014) Additive manufacturing technologies. vol 17. Springer, New York
2. Kamath C, El-dasher B, Gallegos GF, King WE, Sisto A (2014) Density of additively-manufactured, 316L SS parts using laser powder-bed fusion at powers up to 400 W. Int J Adv Manuf Technol 74(1–4):65–78
3. Cheng B, Lydon J, Cooper K, Cole V, Northrop P, Chou K (2018) Infrared thermal imaging for melt pool analysis in SLM: a feasibility investigation. Virtual Phys Prototyping 13(1):8–13
4. Cheng B, Lydon J, Cooper K, Cole V, Northrop P, Chou K (2018) Melt pool sensing and size analysis in laser powder-bed metal additive manufacturing. J Manuf Process 32:744–753
5. Criales LE, Arısoy YM, Lane B, Moylan S, Donmez A, Özel T (2017) Laser powder bed fusion of nickel alloy 625: experimental investigations of effects of process parameters on melt pool size and shape with spatter analysis. Int J Mach Tools Manuf 121:22–36
6. Smurov I (2001) Pyrometry applications in laser machining. Laser-Assisted Microtechnology 2000. vol 4157. International Society for Optics and Photonics
7. Doumanidis C, Kwak Y-M (2001) Geometry modeling and control by infrared and laser sensing in thermal manufacturing with material deposition. J Manuf Sci Eng 123(1):45–52
8. Smurov I, and Ignatiev M (1996) Real time pyrometry in laser surface treatment. Laser Processing: Surface Treatment and Film Deposition. Springer, Dordrecht 529–564
9. Bayle F, Doubenskaia M (2008) Selective laser melting process monitoring with high speed infra-red camera and pyrometer. Fundamentals of laser assisted micro-and nanotechnologies. vol. 6985. International Society for Optics and Photonics
10. Doubenskaia M, Pavlov M, Chivel Y (2010) Optical system for on-line monitoring and temperature control in selective laser melting technology. Key Eng Mater 437:458–461. https://doi.org/10.4028/www.scientific.net/KEM.437.458
11. Islam M, Purtonen T, Piili H, Salminen A, Nyrhilä O (2013) Temperature profile and imaging analysis of laser additive manufacturing of stainless steel. Phys Procedia 41(Supplement C):835–842. https://doi.org/10.1016/j.phpro.2013.03.156
12. Chivel Y, Smurov I (2010) On-line temperature monitoring in selective laser sintering/melting. Phys Procedia 5(Part B):515–521. https://doi.org/10.1016/j.phpro.2010.08.079
13. Pavlov M, Doubenskaia M, Smurov I (2010) Pyrometric analysis of thermal processes in SLM technology. Phys Procedia 5:523–531. https://doi.org/10.1016/j.phpro.2010.08.080
14. Chivel Y (2013) Optical in-process temperature monitoring of selective laser melting. Phys Procedia 41(supplement C):904–910. https://doi.org/10.1016/j.phpro.2013.03.165
15. Furumoto T, Ueda T, Alkahari MR, Hosokawa A (2013) Investigation of laser consolidation process for metal powder by two-color pyrometer and high-speed video camera. Cirp Ann-Manuf Techn 62(1):223–226. https://doi.org/10.1016/j.cirp.2013.03.032
16. Renken V, Lübbert L, Blom H, von Freyberg A, Fischer A (2018) Model assisted closed-loop control strategy for selective laser melting. Procedia CIRP 74:659–663
17. Renken V, von Freyberg A, Schünemann K, Pastors F, Fischer A (2019) In-process closed-loop control for stabilising the melt pool temperature in selective laser melting. Prog Addit Manuf:1–11
18. DeWitt DP, Nutter GD (1988) Theory and practice of radiation thermometry. Wiley, New York
19. Doubenskaia M, Grigoriev S, Zhirnov I, Smurov I (2016) Parametric analysis of SLM using comprehensive optical monitoring. Rapid Prototyp J 22(1):40–50. https://doi.org/10.1108/rpj-04-2014-0046
20. Boley C, Khairallah S, Rubenchik A (2015) Calculation of laser absorption by metal powders in additive manufacturing. Appl Opt 54(9):2477–2482
21. Tran H-C, Lo Y-L (2018) Heat transfer simulations of selective laser melting process based on volumetric heat source with powder size consideration. J Mater Process Technol 255:411–425
22. Roberts I, Wang C, Esterlein R, Stanford M, Mynors D (2009) A three-dimensional finite element analysis of the temperature field during laser melting of metal powders in additive layer manufacturing. Int J Mach Tools Manuf 49(12):916–923

23. Yin J, Zhu H, Ke L, Hu P, He C, Zhang H, Zeng X (2016) A finite element model of thermal evolution in laser micro sintering. Int J Adv Manuf Technol 83(9–12):1847–1859
24. Tran H-C, Lo Y-L, Huang M-H (2017) Analysis of scattering and absorption characteristics of metal powder layer for selective laser sintering. IEEE/ASME Trans Mechatron 22(4):1807–1817
25. Cengel Ya, Ghajar AJ, and Ma. H (2015) Heat and Mass Transfer Fundamentals & Applications. McGraw-Hill
26. Foroozmehr A, Badrossamay M, Foroozmehr E, Si G (2016) Finite element simulation of selective laser melting process considering optical penetration depth of laser in powder bed. Mater Des 89: 255–263. https://doi.org/10.1016/j.matdes.2015.10.002
27. Hodge N, Ferencz R, Solberg J (2014) Implementation of a thermomechanical model for the simulation of selective laser melting. Comput Mech 54(1):33–51
28. Gusarov A, Yadroitsev I, Bertrand P, Smurov I (2009) Model of radiation and heat transfer in laser-powder interaction zone at selective laser melting. J Heat Transf 131(7):072101
29. Streek A, Regenfuss P, Exner H (2013) Fundamentals of energy conversion and dissipation in powder layers during laser micro sintering. Phys Procedia 41:858–869
30. Wang X, Laoui T, Bonse J, Kruth J-P, Lauwers B, Froyen L (2002) Direct selective laser sintering of hard metal powders: experimental study and simulation. Int J Adv Manuf Technol 19(5):351–357
31. King WE, Barth HD, Castillo VM, Gallegos GF, Gibbs JW, Hahn DE, Kamath C, Rubenchik AM (2014) Observation of keyhole-mode laser melting in laser powder-bed fusion additive manufacturing. J Mater Process Technol 214(12):2915–2925
32. Mills KC (2002) Recommended values of thermophysical properties for selected commercial alloys. Woodhead Publishing